A conservative formulation of the $k - \epsilon$ turbulence model for shock-turbulence interaction

Krishnendu Sinha* and S. J. Balasridhar†

Indian Institute of Technology Bombay, Mumbai, 400076, India.

Abstract

Reynolds-averaged turbulence models can result in large numerical error at flow discontinuities like shock waves. This is due to the non-conservative nature of the source terms in the governing equations. In this paper, the $k - \epsilon$ turbulence model is used to compute canonical interaction of a normal shock with homogeneous isotropic turbulence. The characteristics of the non-conservative error is studied as a function of shock strength, grid resolution and upstream turbulence level. The model equations are cast in an equivalent conservation form that gives physically consistent results at a shock wave. The predicted amplifications of turbulent kinetic energy and its dissipation rate match DNS data and linear theory estimates over a range of Mach numbers.

Nomenclature

b_1'	=	shock-unsteadiness damping parameter
c_0, c_1, c_2	=	$k - \epsilon$ model parameters
f, g	=	new turbulence variables
k	=	turbulent kinetic energy
M	=	Mach number
M_t	=	turbulent Mach number
Re_λ	=	Reynolds number based on Taylor microscale
u	=	fluid velocity
x	=	shock-normal direction
δ	=	computed mean shock thickness
ϵ	=	turbulent dissipation rate
κ_0	=	wavenumber corresponding to most energetic scale
λ	=	Taylor microscale

*Associate Professor, Department of Aerospace Engineering, Senior AIAA Member.
†Graduate student, Department of Aerospace Engineering.

μ	=	molecular viscosity
μ_T	=	turbulent eddy viscosity
ρ	=	fluid density
$\sigma_k, \sigma_\epsilon$	=	Prandtl numbers for k and ϵ
subscripts		
0	=	inlet station
1	=	upstream of shock wave
2	=	downstream of shock wave

I. Introduction

Interaction of shock wave with turbulent boundary layers is common in many high-speed flows. Examples include deflected control surfaces, supersonic and hypersonic inlet ducts, multi-body aerodynamics and wing-body junctions. Presence of strong shock waves causes boundary layer separation, which can generate additional shocks and expansion waves. Shear layer reattachment downstream of the shock interaction often leads to localized high pressure and heat flux to the vehicle surface. A separation bubble inside an inlet duct acts as a blockage to the flow and can cause unstart. Accurate numerical prediction of shock-boundary layer interaction (SBLI) flows is a challenging task, especially in the presence of strong shock waves. Several research efforts[1−4] have been directed towards this goal. See Refs. 5 and 6 for a comprehensive survey of previous work.

The interaction of turbulent fluctuations in the boundary layer with the shock wave lies at the heart of these phenomena. Shock-turbulence interaction has therefore been the focus of several studies, some of which are discussed below. Homogeneous isotropic turbulence passing through a normal shock is possibly the most fundamental shock-turbulence interaction. The mean flow is one dimensional and steady, and therefore uniform upstream and downstream of the shock wave. The jump in the mean flow quantities across the shock is governed by the Rankine-Hugoniot relations. Compared to shock-boundary layer interaction, the model problem does not have additional complexity due to the flow separation, stream line curvature and boundary layer velocity gradients.

Shock-homogeneous turbulence interaction has been extensively studied using direct numerical simulation.[7−10] This canonical interaction is also amenable to theoretical analysis using rapid distortion theory[11,12] and linear interaction analysis.[13,14] Some limited experimental data is also available in literature.[15] In spite of the geometrical simplicity, the model problem exhibits a range of physical effects, like, generation of acoustic waves, baroclinic torques and unsteady shock oscillations. Physical insight obtained in this canonical problem has proved useful in developing advanced turbulence models for shock-turbulence interaction.[16−18]

Figure 1, reproduced from Ref. 18, shows the variation of turbulent kinetic energy k as homogeneous

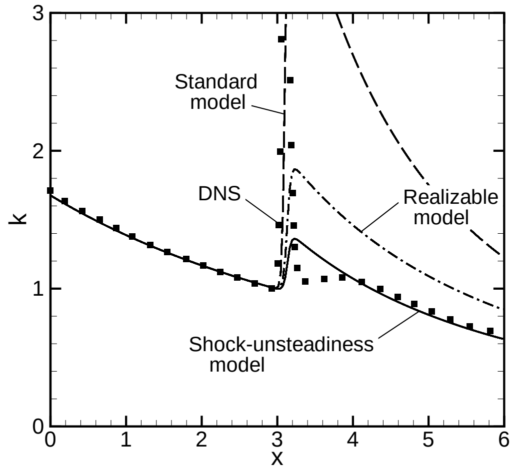

Figure 1: Evolution of turbulent kinetic energy k in the interaction of homogeneous turbulence with a normal shock at Mach 1.5. Different versions of the $k-\epsilon$ model are compared with DNS data.[9]

isotropic turbulence interacts with a nominally normal shock wave. Here, x is the shock-normal direction, and the shock is located at $x = 3$. The mean flow Mach number upstream of the shock is 1.5, the turbulent Mach number is 0.17 and the Reynolds number based on Taylor micro-scale is 6.7. The data corresponds to the direct numerical simulation (DNS) of Jamme *et al.*,[9] where the incoming turbulence field is primarily composed of vortical fluctuations. The magnitude of thermodynamic fluctuations is relatively small.

The turbulent kinetic energy plotted in Fig. 1 is normalized by its value immediately upstream of the shock. A characteristic length of 2λ is used for normalizing the shock-normal distance, where λ is the Taylor microscale in the incoming turbulent flow. In the absence of mean velocity gradient upstream of the shock, the turbulent kinetic energy (TKE) decays from its inlet value. There is an increase in turbulence level across the shock, followed by further decay in the downstream flow. An amplification of the turbulent dissipation rate at the shock results in a faster decay of TKE behind the shock wave. Large values of turbulent kinetic energy are reported in the vicinity of the shock wave. These are artifact of the unsteady shock oscillation, and do not represent turbulent fluctuations.[8]

Computation of the above test case using Reynolds-averaged Navier-Stokes (RANS) equations is also presented in the figure. RANS approach computes the mean flowfield and includes the effect of turbulent fluctuations using a turbulence model. It is extensively used in engineering predictions of shock-turbulent boundary layer interaction. Conventional turbulence models like standard $k-\epsilon$ and $k-\omega$ models predict high amplification of turbulence across the shock (see Fig. 1). Over-prediction of post-shock turbulent kinetic energy, and consequently a high turbulent viscosity downstream of the shock often leads to delayed flow separation in shock-turbulent boundary layer interactions.[19] This can result in significant error in the pressure and surface heat flux predictions.[20] Compressibility corrections,[21] in the form of dilatational dissipation and pressure dilatation, do not improve turbulence levels significantly.[16] Further, they deteriorate model predictions in the upstream boundary layer, and therefore are not preferred in SBLI flows.[22]

The over-amplification of turbulent kinetic energy by the standard $k - \epsilon$ model is due to excessive production of turbulence at the shock wave. It is argued (in Ref. 16) that the high level of turbulence production is caused by the break down of the eddy-viscosity assumption in the highly non-equilibrium region of a shock wave. Suppressing eddy viscosity, for example, by a realizable model,[23] brings down the post-shock turbulence level, but the predictions are still appreciably higher than DNS data (see Fig. 1).

Sinha *et al.*[16] study the physical processes involved in shock/homogeneous turbulence interaction using linearized governing equations. They identify a damping effect of the unsteady shock oscillations on TKE amplification, and develop a model for this effect. The following k-equation is thus proposed for canonical shock/turbulence interaction.

$$\bar{\rho}\tilde{u}\frac{\partial k}{\partial x} = -\frac{2}{3}\bar{\rho}k\frac{\partial \tilde{u}}{\partial x}(1 - b_1') - \bar{\rho}\epsilon\,, \tag{1}$$

where the parameter $b_1' = b_{1,\infty}\left(1 - e^{1-M}\right)$ represents shock-unsteadiness effect and $b_{1,\infty} = 0.4$ is its high Mach number limiting value. Also, the turbulent viscosity is suppressed in the production term, so as to minimize the error due to the limitations in the Boussinesq approximation. Setting $\mu_T = 0$ yields the isotropic form of the Reynolds stress $\widetilde{u''^2} = 2k/3$ at the shock. The ϵ-equation is also modified in a similar way.

Computation of the Mach 1.5 shock/homogeneous turbulence interaction using the shock-unsteadiness model shows good match with the post-shock DNS data. We note that there is a non-monotonic variation in turbulent kinetic energy immediately downstream of the shock wave ($3 < x < 4$). This is due to the decay of acoustic energy generated at the shock and its transfer to the kinetic form. The turbulence models do not reproduce this transfer between the acoustic and vortical modes, but its net effect on TKE amplification is included in the shock-unsteadiness model.

A comparison of turbulence amplification for varying shock strength is shown in Fig. 2, reproduced from Ref. 16. The peak TKE value predicted by the different turbulence models, in the limit of vanishing turbulent dissipation at the shock, is evaluated against linear interaction analysis (LIA) results. The theory assumes linear interaction of incoming turbulent fluctuations with the shock, which is modeled as a discontinuity. Viscous effects are neglected to compute the jump in turbulence quantities across the shock wave. TKE and ϵ amplifications obtained from DNS of Larsson and Lele[10] are found to match LIA far-field predictions, which are used here for model evaluation.

The $k-\epsilon$ model with $\mu_T = 0$ matches LIA results for weak shocks ($M < 1.3$). The model, however, over-predicts TKE for stronger shock waves (see Fig. 2(a)). The realizable $k-\epsilon$ model predictions are significantly higher than theory for all shock strengths. By comparison, the shock-unsteadiness model matches the theoretical predictions for the entire range of Mach numbers. Similar results for the amplification of turbulent

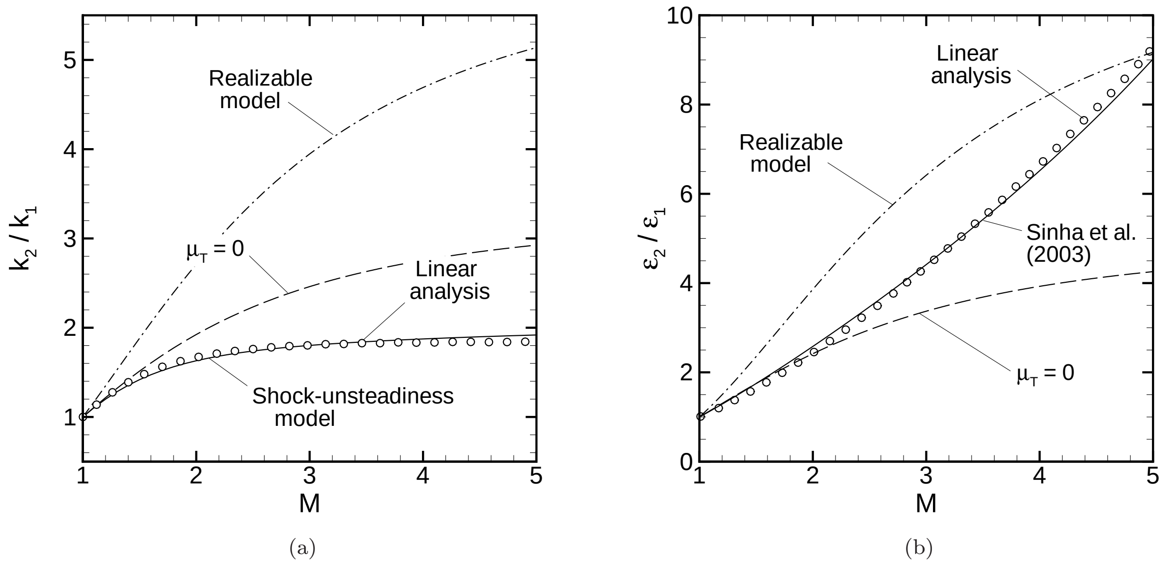

Figure 2: Amplification in turbulent kinetic energy and turbulent dissipation rate in shock/homogeneous turbulence interaction as a function of upstream mean flow Mach number. Different turbulence models are compared to linear theory predictions.

dissipation rate ϵ are shown in Fig. 2(b), where the model proposed by Sinha *et al.*[16] reproduces LIA results closely. The realizable and $\mu_T = 0$ models, on the other hand, exhibit qualitative and quantitative disagreement with the linear theory. A detailed analysis and modeling of the ϵ-amplification is presented in a recent paper by Sinha.[18]

The standard $k - \epsilon$ model solution is found to be highly sensitive to the grid-point distribution at the shock. As the grid is refined to get a thinner shock wave, the post-shock k and ϵ levels increase dramatically (see Fig. 12 in Ref. 18). There is no unique grid-independent solution of the standard $k - \epsilon$ model equations for the current shock-turbulence interaction. It is, therefore, not included in Fig. 2.

The realizable $k - \epsilon$ model, the shock-unsteadiness model and the $k - \epsilon$ model with $\mu_T = 0$ can be analytically integrated across the shock, if the effect of turbulent dissipation is neglected in the region of the shock wave. The closed-form solutions thus obtained are plotted in Fig. 2, and can be assumed to hold in the inviscid limit or in high Reynolds number flows. As shown below, the CFD solutions of these $k - \epsilon$ models should approach their respective exact integration limits as the grid is progressively refined. This is, however, contrary to the observations made. The $k - \epsilon$ solution, in some cases, do not show a converging trend with successive grid refinement. Also, the peak k and ϵ values obtained on fine grids are found to differ significantly from the analytical solution.

The non-physical behavior of the $k - \epsilon$ solutions are most prominent for strong shock waves, and are probably caused by the non-conservative nature of the source terms in the governing equations. In particular, the source terms contain non-conservative derivatives of the flow variables, and the corresponding discretization error attain large values in a flow discontinuity. Further, the error do not decrease in magnitude with successive grid refinement, as observed for smooth solutions. In some cases, for example, strong shock waves, the error can amplify on fine grids to yield unrealistic values of k and ϵ at the shock.

In this paper, we systematically study the numerical characteristics of the $k-\epsilon$ solution for canonical shock/turbulence interaction. A finite-volume based CFD code is used for the simulations. The evolution of k and ϵ across the normal shock wave is presented for a range of upstream mean flow Mach numbers. The upstream turbulence quantities correspond to the conditions for which DNS data is reported by Larsson and Lele.[10] Effect of grid refinement on k- and ϵ-amplification at the shock is quantified. Results are also presented for varying upstream values of the turbulence variables.

An alternate conservative form of the $k-\epsilon$ equations is derived and implemented in the finite-volume code. The advantages of the new formulation over the traditional non-conservative $k-\epsilon$ equations is shown for the chosen test cases. The effect of shock strength, grid sensitivity and variability due to changes in inlet conditions are investigated. Finally, future direction towards extending the conservative $k-\epsilon$ formulation to the simulation of complex high-speed flows is discussed.

II. Governing Equations

In this section, the turbulence transport equations in the standard $k-\epsilon$ model are presented, and the non-physical behavior of the production terms is highlighted. The physics-based shock-unsteadiness $k-\epsilon$ model, and the non-conservative nature of the turbulent source terms are discussed next. The model equations are then written in an alternate form to eliminate the non-conservative source terms. The extension of the new conservative formulation to other turbulence models, including the recent stress-limited $k-\omega$ model of Wilcox,[24] is described subsequently.

A. Standard $k-\epsilon$ model and its variations

The standard $k-\epsilon$ model[25] applied to the steady one-dimensional interaction of homogeneous isotropic turbulence with a normal shock wave takes the following form.

$$\bar{\rho}\tilde{u}\frac{\partial k}{\partial x} = -\bar{\rho}\widetilde{u''^2}\frac{\partial \tilde{u}}{\partial x} - \bar{\rho}\epsilon + \frac{\partial}{\partial x}\left[\left(\bar{\mu} + \frac{\mu_T}{\sigma_k}\right)\frac{\partial k}{\partial x}\right] \tag{2}$$

$$\bar{\rho}\tilde{u}\frac{\partial \epsilon}{\partial x} = -c_1\bar{\rho}\widetilde{u''^2}\frac{\epsilon}{k}\frac{\partial \tilde{u}}{\partial x} - c_2\frac{\bar{\rho}\epsilon^2}{k} + \frac{\partial}{\partial x}\left[\left(\bar{\mu} + \frac{\mu_T}{\sigma_\epsilon}\right)\frac{\partial \epsilon}{\partial x}\right] \tag{3}$$

where overbar and tilde represent Reynolds and Favre averaging, respectively and double prime corresponds to Favre-fluctuations. The normal Reynolds stress $\widetilde{u''^2}$ is given by the Boussinesq approximation,

$$-\bar{\rho}\widetilde{u''^2} = \frac{4}{3}\mu_T\frac{\partial \tilde{u}}{\partial x} - \frac{2}{3}\bar{\rho}k, \tag{4}$$

where $\mu_T = c_\mu \bar{\rho} k^2/\epsilon$ and $c_\mu = 0.09$. As noted earlier, compressibility corrections are not included in the $k - \epsilon$ equations.

The first term on the right-hand side of (2) represents production of turbulence due to mean-flow gradients, and is responsible for the amplification in k across a shock. The production of k is proportional to $(\partial\tilde{u}/\partial x)^2$, and therefore takes very large values at a shock wave. Integration of the source term across the mean shock wave yields a contribution proportional to $1/\delta$ towards TKE amplification. Here, δ is the mean shock thickness computed in a CFD simulation, and it decreases as the grid-point density at the shock is increased. The jump in TKE, therefore, increases on successive grid refinement, and does not reach a grid-converged value. The production term in the ϵ-equation (3) also exhibits a similar non-physical trend, and it has been discussed in previous work.[18]

The second term in each equation represents turbulent dissipation and determines the decay rate of turbulence on either side of the shock wave. The last term corresponds to viscous and turbulent diffusion. They have negligible contribution at a shock wave, and are therefore neglected.

Sinha *et al.*[16] propose a shock-unsteadiness correction to the $k - \epsilon$ model, as described above. The eddy viscosity is set to zero in Eq. (4) and an additional parameter b_1' is used to model the damping of TKE due to unsteady shock motion. The resulting k-equation can be written as

$$\bar{\rho}\tilde{u}\frac{\partial k}{\partial x} = -\frac{2}{3}c_0\bar{\rho}k\frac{\partial \tilde{u}}{\partial x} - \bar{\rho}\epsilon\,, \tag{5}$$

where the effects of production and shock-unsteadiness damping are combined into $c_0 = 1 - b_1'$. The modified ϵ-equation is given by

$$\bar{\rho}\tilde{u}\frac{\partial \epsilon}{\partial x} = -\frac{2}{3}c_1\bar{\rho}\epsilon\frac{\partial \tilde{u}}{\partial x} - c_2\frac{\bar{\rho}\epsilon^2}{k}\,, \tag{6}$$

where $c_1 = 1.2 + 0.21M$ and $c_2 = 1.2$ are model parameters. See Ref. 18 for additional details.

The convection terms on the left-hand side of (5) and (6) represent the evolution of k and ϵ in the shock-normal direction. They are balanced by the source terms on the right-hand side. The first term results in turbulence amplification at the shock, and the second term corresponds to dissipation effect. The turbulent dissipation terms cause reduction in k and ϵ at the shock wave, which scale as

$$\Delta k \sim -\frac{\epsilon}{\tilde{u}}\delta \quad \text{and} \quad \Delta\epsilon \sim -c_2\frac{\epsilon^2}{\tilde{u}k}\,\delta\,. \tag{7}$$

The mean shock thickness δ in a RANS solution is proportional to the grid size. The dissipation effect therefore decreases as the shock gets thinner on successive grid refinement. Only exception is for cases where ϵ is large, and they are discussed separately. Neglecting dissipation in (5) and (6), and integrating the resulting equations analytically yields the following amplification in k and ϵ in terms of the mean density ratio across the shock wave.

$$\frac{k_2}{k_1} = \left(\frac{\bar{\rho}_2}{\bar{\rho}_1}\right)^{\frac{2}{3}c_0} \quad \text{and} \quad \frac{\epsilon_2}{\epsilon_1} = \left(\frac{\bar{\rho}_2}{\bar{\rho}_1}\right)^{\frac{2}{3}c_1} \tag{8}$$

The above closed-form solutions are plotted as a function of upstream Mach number and compared with LIA results in Fig. 2. The k-amplification is close to unity for weak shock waves ($M \to 1$), and increases with shock strength. It tends to saturate to a value close to 2 for high Mach number interactions. On the other hand, the amplification in ϵ increases monotonically with shock strength. This is due to an amplification in enstrophy that contributes to the solenoidal dissipation rate. Increase in the mean flow temperature and viscosity at the shock further adds to the ϵ-jump.

The convection terms in (5) and (6) can be written in a conservative form using the Reynolds-averaged mass conservation equation. In a finite-volume approach, the convective fluxes are evaluated at cell interfaces. The corresponding truncation error involves higher-order derivatives of the conserved quantity, for example, $\bar{\rho}\tilde{u}k$ in (5). On integration over the finite-volume cell, we get a leading-order error in terms of the derivatives evaluated at the cell boundaries; see (A.5) in Appendix. These derivative terms take large values in the region of a flow discontinuity. However, contributions from adjacent cells cancel at the common interfaces. When all the cells spanning a shock wave are taken together, the net error is a function of the higher-order derivatives (A.10) evaluated in a region of smooth flow solution, outside the shock wave. The exact integrated effect across the shock is thus recovered, as the leading error term vanishes on successive grid refinement.

On the other hand, the production terms in (5) and (6) are non-conservative. A symmetric second-order discretization of the corresponding velocity derivative is used in the current CFD implementation. The corresponding error term involves integration of $\partial^3\tilde{u}/\partial x^3$ over the finite-volume cell (A.8). Contrary to the convective fluxes discussed above, these error terms from adjacent cells add up. Their overall contribution across a shock wave, therefore, involves high-order velocity derivatives evaluated in the region of the flow discontinuity; see (A.11) in Appendix. These derivatives scale as $1/\delta^3$, and result in large error in a shock wave. Further, thinner shocks obtained on finer grids can lead to larger error than in coarse grid simulations. This often results in non-physical trends in k and ϵ amplification with successive grid refinement.

The simulation results presented in the next section highlight several aspects of the non-conservative $k-\epsilon$ equations. It is shown that the numerical results are different, both qualitatively and quantitatively, from the exact integration (8). Alternate forms of (5) and (6) are presented below that eliminate the non-conservative source terms.

B. Conservative Formulation

Noting that $k \propto \rho^{\frac{2}{3}c_0}$ across the shock wave in the inviscid limit, we define

$$f = k\rho^{-\frac{2}{3}c_0}$$

that is constant across a shock. Here, the overbar on ρ is dropped to avoid potential conflict with the sign of the exponent. A transport equation for f can be derived by multiplying (5) by $\rho^{-\frac{2}{3}c_0}$

$$\rho^{-\frac{2}{3}c_0}\ \rho\tilde{u}\frac{\partial k}{\partial x} = -\frac{2}{3}c_0\rho k\frac{\partial \tilde{u}}{\partial x}\rho^{-\frac{2}{3}c_0} - \rho\epsilon\rho^{-\frac{2}{3}c_0}\,. \tag{9}$$

Mass conservation across the shock wave is used to write

$$\rho\tilde{u}k\frac{\partial}{\partial x}\rho^{-\frac{2}{3}c_0} = \frac{2}{3}c_0\rho k\frac{\partial \tilde{u}}{\partial x}\rho^{-\frac{2}{3}c_0}\,. \tag{10}$$

Adding (9) and (10), we get

$$\rho\tilde{u}\frac{\partial f}{\partial x} = -\rho\epsilon\ \rho^{-\frac{2}{3}c_0}\,, \tag{11}$$

where the source term with non-conservative derivative is eliminated. Note that the quantity f is continuous across the shock, and the convective term on the left-hand side is conservative. It is of the form h in (A.1) and the corresponding discretization error exhibits a telescoping effect at the cell interfaces, as discussed above. We thus get a well-behaved numerical solution at a flow discontinuity.

Similar development for the ϵ-equation leads to a new variable,

$$g = \epsilon\rho^{-\frac{2}{3}c_1}$$

and the corresponding transport equation is

$$\rho\tilde{u}\frac{\partial g}{\partial x} = -c_2\frac{\rho\epsilon^2}{k}\ \rho^{-\frac{2}{3}c_1}. \tag{12}$$

Substituting $\epsilon = g\rho^{\frac{2}{3}c_1}$ and $k = f\rho^{\frac{2}{3}c_0}$, the above equations can be cast into the following form,

$$\rho\tilde{u}\frac{\partial f}{\partial x} = -\rho g\ \rho^{\frac{2}{3}(c_1-c_0)}, \tag{13}$$

$$\rho\tilde{u}\frac{\partial g}{\partial x} = -c_2\frac{\rho g^2}{f}\ \rho^{\frac{2}{3}(c_1-c_0)}, \tag{14}$$

which are similar to the original equations (5) and (6), except for the absence of the production terms. The dissipation terms retain their original form with an additional factor of $\rho^{\frac{2}{3}(c_1-c_0)}$.

The development of the $k-\epsilon$ equations presented above can be easily extended to the $k-\omega$ model. The production terms in the standard $k-\omega$ equations have a form similar to those in (2) and (3). They also exhibit non-physical turbulence amplification at a shock wave. Wilcox[24] presents a stress-limiter $k-\omega$ model, which limits TKE production at a shock. For a normal shock, the corresponding k-equation can be written in the form of (5) with $c_0 = 1.725$. It can therefore be transformed to an equivalent conservative form (13) following the steps delineated above. Other two-equation turbulence models like SST,[26] realizable

$k-\epsilon$ models of Durbin[27], Thivet *et al.*[23] and Shih *et al.*[28], as well as the recent shock-turbulence $k-\epsilon$ model[18] can also be developed in a similar way.

III. Simulation Methodology

The Reynolds-averaged Navier Stokes equations are solved for the mean flow, and the two-equation $k-\epsilon$ model is used for turbulence closure.[25] The flow variables are normalized by the mean density and mean speed of sound upstream of the shock wave. The most energetic wave number κ_0 in the incoming turbulence field is taken as the characteristic length scale. A finite-volume approach is used, where the turbulence model equations are fully coupled with the mean flow conservation equations.[29] The inviscid fluxes are computed with a modified, low-dissipation form of the Steger-Warming flux-vector splitting method.[30] The flux vector F is evaluated at each cell face using the conserved variables vector U stored at cell centers. The Jacobian $A = \partial F/\partial U$ is diagonalized as

$$A = T^{-1}\Lambda\, T$$

where Λ is a diagonal matrix consisting of the eigen values of the system, and T^{-1} and T are the left and right eigen vector matrices. The positive and negative eigen values are used to split the Jacobian matrix into A^+ and A^-. The flux vector is thus evaluated as a combination of the positive and negative flux contributions from the left and right side of a cell face $i+1/2$.

$$F_{i+1/2} = A^+U_l + A^-U_r$$

For a first-order flux evaluation, $U_l = U_i$ and $U_r = U_{i+1}$. Higher-order reconstruction is achieved by using the MUSCL approach.

The viscous fluxes due to molecular and turbulent diffusivities are computed using a second-order central difference method applied at each cell face. The turbulent source terms are evaluated at the cell centers, where the velocity gradients in the production terms are discretized using a central difference scheme akin to that presented in Appendix. The implicit data parallel line relaxation method of Wright *et al.*[31] is employed for time integration and the code has been used successfully in several supersonic and hypersonic applications. Some representative results are presented in Refs. 19, 20 and 32.

The canonical shock-turbulence interaction flows computed in this work are listed in Table 1. The mean flow Mach number for the test cases range from low supersonic to nearly the hypersonic limit. The incoming turbulence field is assumed to be primarily composed of vortical fluctuations. There is negligible variation in the thermodynamics variables upstream of the shock wave. DNS data for a limited number of cases is presented by Larsson and Lele,[10] where the turbulent Mach number immediately upstream of the shock wave is 0.22. The Reynolds number based on Taylor microscale is 40 at this location. The normalized values

Table 1: Mean and turbulent flow quantities for the interaction of homogeneous turbulence with a normal shock. The normalized values of k and ϵ correspond to the inflow station.

M	k_0	ϵ_0	DNS source
1.5	2.88×10^{-2}	11.3×10^{-4}	Larsson & Lele[10]
2.0	2.76×10^{-2}	10.7×10^{-4}	
2.5	2.69×10^{-2}	10.4×10^{-4}	Larsson & Lele[10]
2.75	2.66×10^{-2}	10.3×10^{-4}	
3.0	2.64×10^{-2}	10.2×10^{-4}	
3.5	2.61×10^{-2}	10.0×10^{-4}	Larsson & Lele[10]
4.25	2.57×10^{-2}	9.9×10^{-4}	
4.7	2.56×10^{-2}	9.8×10^{-4}	Larsson & Lele[10]

of TKE and turbulent dissipation rate are thus calculated as,

$$k_1 = \frac{M_t^2}{2} \quad \text{and} \quad \epsilon_1 = \frac{5}{\sqrt{3}} \frac{M_t^3}{Re_\lambda} \frac{1}{\kappa_0 \lambda} \tag{15}$$

A non-dimensional value of the Taylor microscale $\kappa_0\lambda = 0.84$ yields $k_1 = 0.0242$ and $\epsilon_1 = 9.15 \times 10^{-4}$. These are extrapolated to the inlet station using the decay relations for homogeneous isotropic turbulence.

The computational domain, between the inlet ($x = -7.6$) and exit ($x = 29.6$) stations, is discretized using 200 equi-spaced points in the shock-normal direction. The effect of grid refinement is discussed in detail in the following section. Free-stream and inlet conditions, listed in Table 1, are specified at the upstream boundary. Rankine-Hugoniot jump relations are used to obtain the mean flow back pressure, and extrapolation condition is employed for the turbulence variables at the exit boundary. The mean flow is initialized to a hyperbolic tangent profile, and the turbulence variables are set to their inlet values in the entire domain.

The original CFD code is based on the conventional form of the turbulence model equations (2) and (3). The conservation form of the model equations is incorporated by interpreting the turbulence variables in the code as f and g, in stead of k and ϵ. Minimal changes are then required to the CFD code to implement the conservative form of the $k - \epsilon$ equations (13) and (14). These are listed below.

1. The initial and boundary conditions for k and ϵ are transformed to the new variables f and g.

2. Computation of the turbulent source terms are modified by dropping the production term and multiplying the dissipation term by a factor $\rho^{\frac{2}{3}(c_1 - c_0)}$.

3. The original turbulence variables k and ϵ are recovered from the converged flowfield solution by invoking the reverse transform.

Note that computation of the convection fluxes are not altered, as they have the same form for the original and new turbulence variables. Further, the diffusive fluxes are not included in the computation, as their contribution is expected to be small in the current shock-turbulence interactions.

IV. Numerical results and comparison

The canonical shock-homogeneous turbulence interaction test cases listed in Table 1 are computed using the traditional non-conservative form of the $k - \epsilon$ equations and the new conservative formulation presented above. Results are evaluated against available DNS data. The amplification in k and ϵ across the shock wave are also compared with the exact solution (8) obtained by direct integration of the $k - \epsilon$ equations in the inviscid limit. Availability of a closed-form solution for the current problem makes it ideal for testing different numerical methods and formulations. Simulation results are documented below, where the important physical and numerical parameters of the problem are varied independently. These include the shock strength in terms of the upstream mean flow Mach number, grid resolution at the shock wave and turbulence level in the upstream flow.

A. Effect of upstream Mach number

Figure 3 presents the evolution of TKE and turbulent dissipation rate for three test cases with varying shock strengths. As earlier, both k and ϵ values are normalized by their values immediately upstream of the shock wave. For an upstream Mach number of 1.5, both the conservative and non conservative models give comparable levels of the post-shock turbulent kinetic energy. They match the DNS data downstream of the shock well. The conservative formulation also matches the ϵ-amplification at the shock, but under-predicts the DNS data in the post-shock flow. The non-conservative formulation, on the other hand, slightly over-predicts the peak turbulent dissipation rate and is closer to the DNS data further downstream.

For the Mach 2.5 case, the conservative form of the model equations match the DNS amplification of k and ϵ in Figs. 3(c) and 3(d). The downstream decay is also reproduced well, except for an over-prediction of the turbulent dissipation rate in the range $0 < x < 6$. This may be because of anisotropy effects that are prominent in the near field; see Ref. 18 for further details. By comparison, the non-conservative formulation yields a higher amplification of TKE (by 12.7 % compared to the conservative results) at the shock. The peak ϵ-level is grossly over-predicted (6.6 times the upstream value) compared to the conservative form and DNS data. Higher post-shock ϵ results in a steeper decay of both TKE and turbulent dissipation rate in the downstream flow.

For the strongest interaction ($M = 3.5$) presented in Figs. 3(e) and 3(f), the conservative formulation results for k and ϵ show the same qualitative trend as in the Mach 2.5 case. The prediction of turbulent dissipation rate matches DNS data at the shock and far downstream. In the near-field ($0 < x < 10$), ϵ is over-predicted and the discrepancy is larger than the Mach 2.5 interaction. As earlier, the over-prediction of the turbulence dissipation rate is due to the physical limitation of the linear-analysis based $k - \epsilon$ model, and it results in a lower TKE downstream of the shock. The amplification in k at the shock is, however, predicted well by the conservative equations.

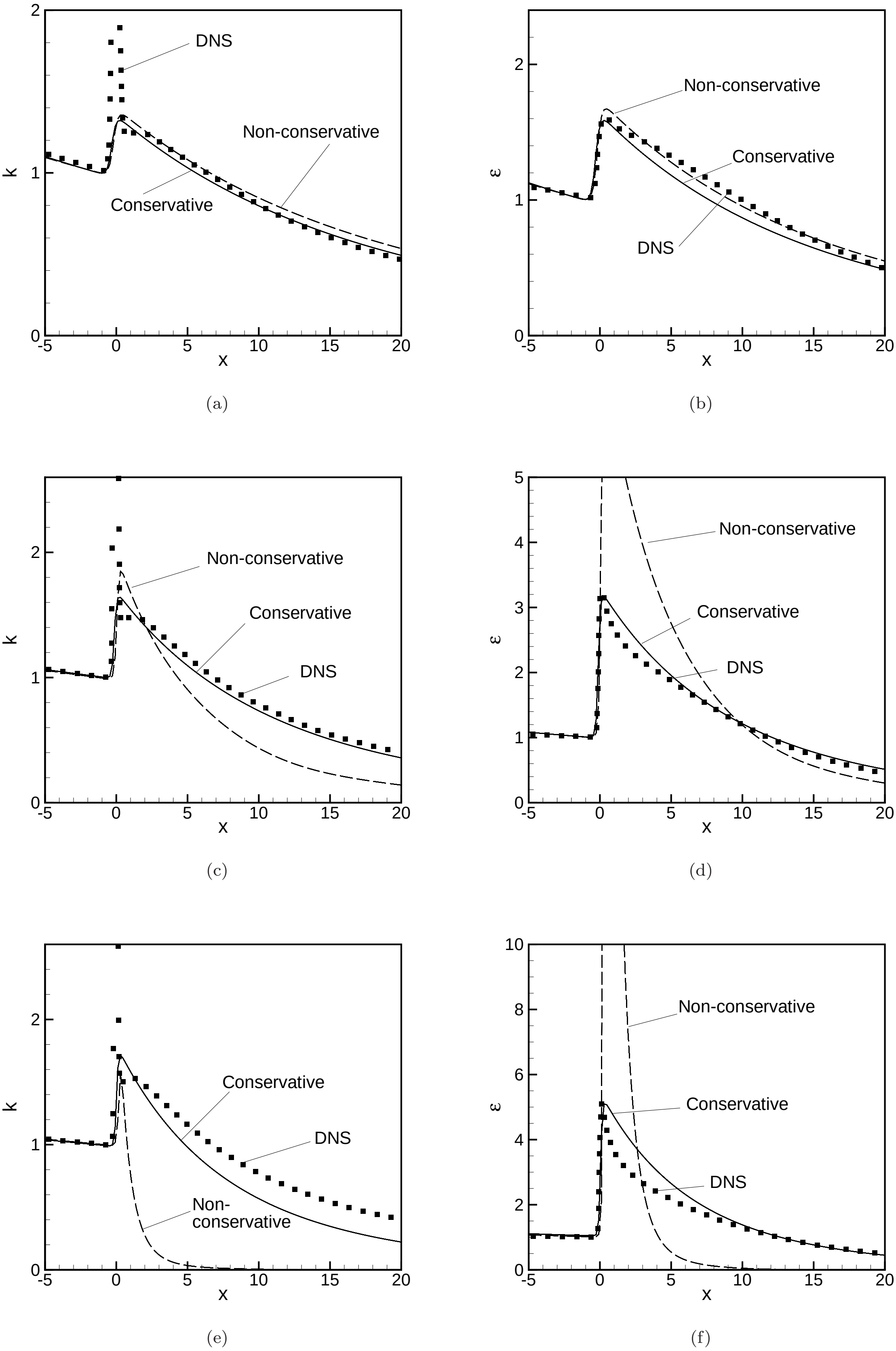

(a) (b) (c) (d) (e) (f)

Figure 3: Variation of TKE and turbulent dissipation rate in shock/homogeneous turbulence interaction at Mach 1.5, (a) and (b); 2.5, (c) and (d); and 3.5, (e) and (f). The solutions computed using non-conservative and conservative formulations of the $k - \epsilon$ turbulence model are compared with DNS data of Larsson and Lele.[10]

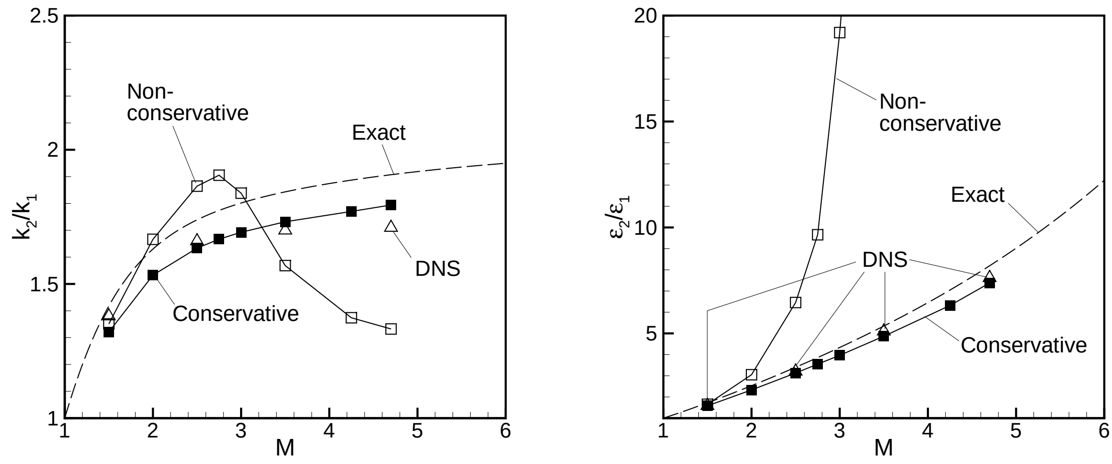

(a)

(b)

Figure 4: Variation in k- and ϵ-amplification with upstream Mach number as computed using the conservative and non-conservative formulations. The numerical predictions are compared with exact inviscid solution (8) and DNS data[10] denoted by Δ.

The non-conservative formulation of the $k-\epsilon$ model predicts a very high ϵ in the Mach 3.5 case. The turbulent dissipation rate is amplified by a factor of 47.6, followed by a rapid decay behind the shock. The jump in TKE at the shock obtained using the non-conservative equations is found to be lower than that predicted by the conservative equations and DNS. This is opposite to the trend observed at lower Mach numbers, and is caused by the high values of ϵ at the shock. In this case, the net turbulent dissipation of k in the region of the shock wave, given by (7), is large enough to cause a significant drop in the peak TKE level obtained in the interaction. Both k and ϵ decay rapidly in the post shock flow to reach negligible values for $x > 10$.

Figure 4 plots the jump in k and ϵ across the shock as a function of the upstream mean flow Mach number. The k-amplification computed using the conservative procedure increases with Mach number and follows the same qualitative trend as the exact integration. The same is true for the ϵ-amplification presented in Fig. 4(b). Both k and ϵ predictions are lower than the inviscid limit (8), because of the effect of turbulent dissipation in the shock region. The dissipation effect (7) is neglected while integrating the respective production terms to arrive at (8). On the other hand, DNS solves the full Navier-Stokes equations including the viscous effects. The amplification in k and ϵ obtained from DNS is therefore lower than the inviscid limit and it is found to be close to the conservative RANS predictions in Figs. 4(a) and 4(b).

The non-conservative formulation of the $k-\epsilon$ turbulence model predicts a higher amplification of turbulent dissipation rate at the shock. The error increases dramatically with Mach number; there is over-amplification by an order in magnitude for the strongest interaction ($M = 4.7$) simulated. The TKE amplification, on the other hand, increases with Mach number for weak and moderately strong shocks, followed by a drop in the peak k value for strong shock waves. The reason is explained earlier as a result of the competing effects of the

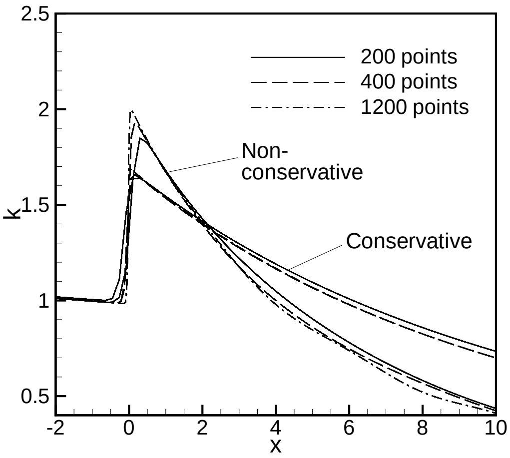

(a)

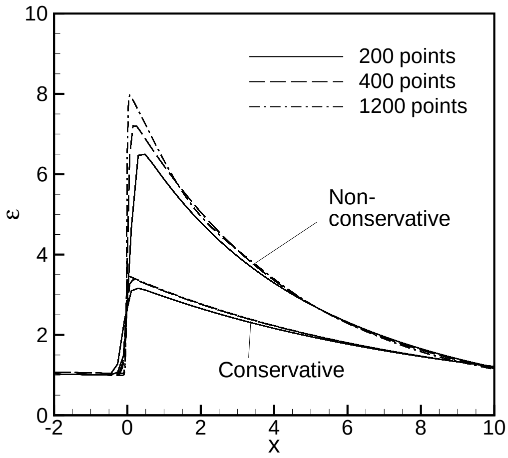

(b)

Figure 5: Evolution of TKE and turbulent dissipation rate in the Mach 2.5 test case for varying number of grid points in the shock-normal direction.

production and dissipation terms in the k-equation. For the strongest interaction ($M = 4.7$), the post-shock k-level is 30% lower than the exact value. More importantly, there is a complete mismatch between the qualitative variation of k_2/k_1 with Mach number obtained using the traditional non-conservative form of the $k - \epsilon$ model and that expected from the direct integration of the equations.

B. Grid sensitivity

The sensitivity of the results presented above to the variation in grid-point density is studied next. The Mach 2.5 test case is computed using three grids – the baseline grid of 200 points and two finer grids of 400 and 1200 points respectively. Grid points are uniformly distributed between the inlet and exit locations, such that the shock-normal grid spacing for the three grids are 0.186, 0.093 and 0.031 respectively.

The TKE and dissipation rate computed using the conservative and non-conservative RANS codes are presented in Fig. 5. The solutions follow the same qualitative trend as earlier, and majority of the variations due to grid refinement are localized in the vicinity of the shock wave. The peak value of ϵ, in Fig. 5(b), obtained using the non-conservative formulation increases on successive refinement. By comparison, the conservative code results show a converging trend; the 1200-point grid yields essentially identical solution to that obtained using 400 points. A similar trend is observed in Fig. 5(a). There is negligible variation in the TKE amplification computed using the conservative formulation on the three successively refined meshes. The non-conservative solutions, on the other hand, show an increase in TKE peak value as the grid is refined. Also, the location of the peak moves closer to $x = 0$ as the shock gets thinner.

The grid sensitivity of the numerical solutions for varying shock strengths is presented in Fig. 6, where the amplification of k and ϵ obtained using the three grids are plotted as a function of upstream Mach

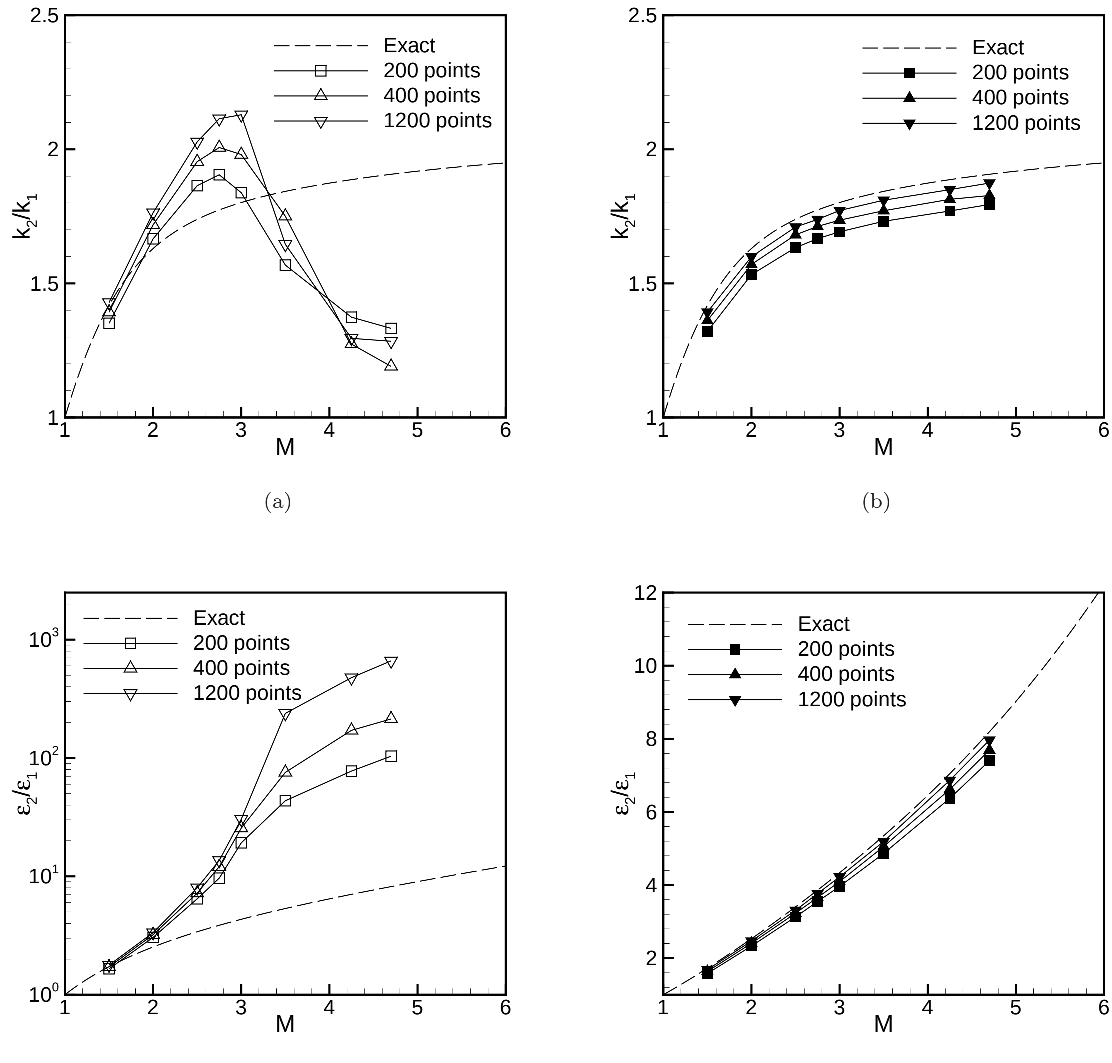

Figure 6: Amplification in TKE and turbulent dissipation rate across a shock wave as a function of upstream Mach number for varying grid-point density – (a) and (c) are non-conservative results; (b) and (d) are obtained using the conservative $k - \epsilon$ equations. Note that a log scale is used in (c).

number. In the conservative case, both k and ϵ amplifications approach the exact inviscid solution as the grid-point density is increased. The discretization error in the convective terms in (5) and (6) are of the form (A.10) in the shock wave, and they decrease (as Δx^2) as the grid spacing is reduced. The effect of turbulent dissipation at the shock scales as per (7), and is proportional to the shock thickness ($\delta \sim \Delta x$). Both the discretization error and the dissipation effect decrease with successive grid refinement; the latter being the dominant contribution at small Δx. Overall, the deviation of the numerical solution from the exact inviscid integration (8) vanishes as $\Delta x \to 0$ on fine grids.

The ϵ-amplification in Fig. 6(c) obtained using the non-conservative formulation exhibits a diverging trend as the computational grid is refined. The deviation from the exact solution increases with shock strength. This is because the error term is proportional to the jump in mean velocity at the shock, as given

Table 2: Turbulence level immediately upstream of the shock wave for varying inlet conditions.

	k_1	M_t	ϵ_1
Twice	0.0484	0.31	2.59×10^{-3}
Baseline	0.0242	0.22	9.15×10^{-4}
Half	0.0121	0.16	3.23×10^{-4}

by (A.9). Further, the amplification in turbulent dissipation rate at a fixed Mach number increases with grid refinement. This can be explained by the $1/\delta^3 \sim 1/\Delta x^3$ variation of the leading velocity derivative in the error term. For the Mach 4.7 case, the finest grid yields a peak value that is more than 600 times the upstream level.

The TKE amplification obtained using the non-conservative formulation also increases with successive grid refinement. Once again, the trend is limited to weak and moderate shock strengths. For strong shocks ($M > 3$), the high ϵ-amplification across the shock dominates over the production effect, resulting in a drop in the post-shock TKE level with increasing Mach number.

C. Effect of upstream turbulence

Simulations are performed by varying the upstream turbulence levels and the sensitivity of the results is analyzed. The value of TKE immediately upstream of the shock is increased by a factor of two compared to the baseline cases presented in Table 1. The turbulent Mach number is thus enhanced by $\sqrt{2}$ and the turbulent dissipation rate increases by a factor of $\sqrt{8}$ to maintain the same value of Re_λ as in the baseline simulation. The corresponding values of k_1 and ϵ_1 are listed in Table 2. Next, the upstream TKE is reduced by a factor of two, which results in a decrease in ϵ_1 by a factor of $\sqrt{8}$. These values are also listed in the table and are used to calculate the different Mach number cases presented above. A 200-point grid is used in all the simulations.

The results obtained for different shock strengths using the conservative $k - \epsilon$ formulation are plotted in Fig. 7. The variation of TKE amplification with Mach number for higher and lower upstream turbulence level have the same qualitative variation as the baseline case. The amplification is higher when the upstream TKE level is half of the baseline value and it is lower for the higher upstream turbulence level. This is because of a corresponding reduction in upstream turbulent dissipation rate ϵ_1 in the simulation where k_1 is decreased. A lower dissipation effect (7) in the shock region results in a higher k_2/k_1 that is closer to the exact inviscid result (8). On the other hand, a higher ϵ_1 in the simulation with higher k_1 shows a larger deviation from the inviscid limit. The amplification in turbulent dissipation rate across the shock, in Fig. 7(b), exhibits a trend identical to the TKE data. The results computed for reduced inlet TKE is again closest to the exact inviscid solution.

The non-conservative simulations also exhibit an increase in turbulence amplification across the shock as

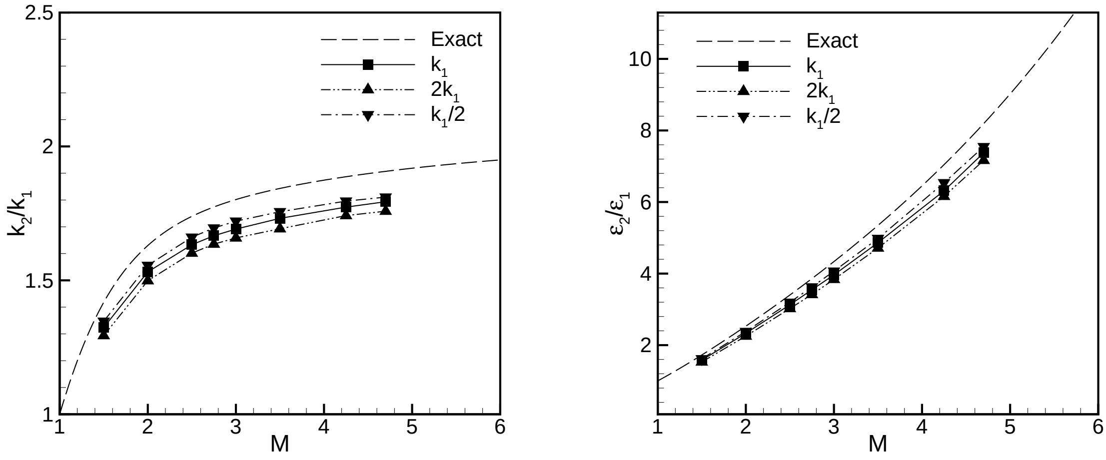

(a)

(b)

Figure 7: Effect of varying inlet turbulence level on the amplification in TKE and turbulent dissipation rate in shock/homogeneous turbulence interaction. The data is computed using the conservative $k-\epsilon$ equations, and plotted as a function of upstream Mach number.

the upstream turbulence level is decreased. The jump k_2/k_1 in Fig. 8(a) attains highest value at $M = 3$ for the simulation with upstream turbulence level half of the baseline condition, whereas it is lowest for the case when incoming k value is increased. TKE amplification for all simulations drop for $M > 3$, as seen earlier. The effect of varying upstream turbulence level is most prominent in Fig. 8(b), which shows large changes in ϵ-amplification at high Mach numbers. Once again, a higher jump ϵ_2/ϵ_1 is observed for lower upstream ϵ_1 and vice-versa.

The foregoing results show that the conservative form of the $k-\epsilon$ turbulence model is able to predict shock-turbulence interaction consistently over a range of upstream Mach numbers. The RANS solution matches DNS data well, and discrepancies in the post-shock turbulence evolution in the near field is due to limitations in the physical modeling. Also, the predicted turbulence amplification across the shock closely follows the analytical solution, which is almost identical to the linear theory predictions (see Fig 2). The deviation from the theoretical curve is due to the effect of turbulent dissipation in a finite thickness shock wave, and its magnitude decreases with successive grid refinement. Thus, the conservative $k-\epsilon$ equations give accurate and physically consistent solution for the shock/homogeneous turbulence interactions considered in this work.

D. Generalization to SBLI flows

Interaction of shock waves with turbulent boundary layers involve additional gradients in the mean flow quantities. Also, the shock is usually oblique to the incoming flow, and may be curved due to Mach number variation in the boundary layer. In order to apply the proposed conservative form of the turbulence model equations to general SBLI configurations, we need to address these and related issues. Some ideas for

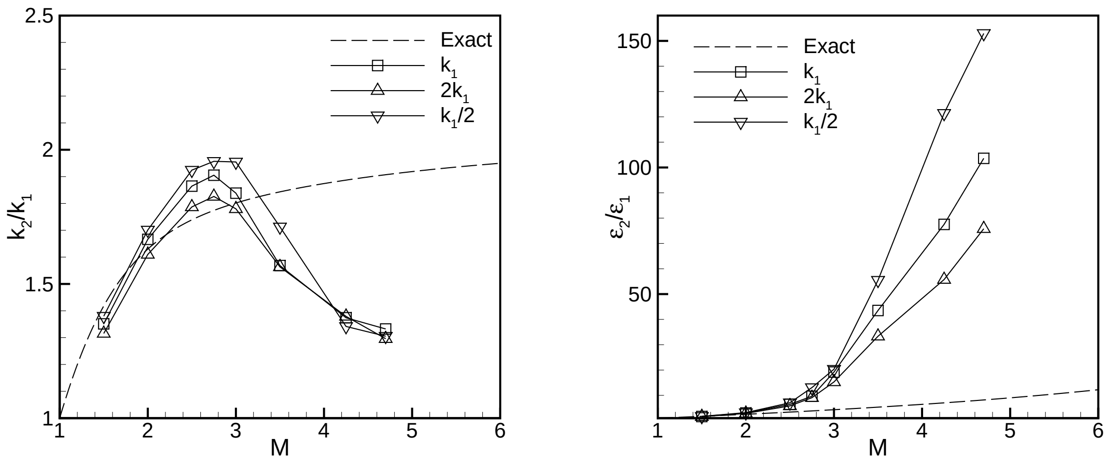

(a) (b)

Figure 8: Amplification in TKE and turbulent dissipation rate across a shock wave as a function of upstream Mach number for varying inlet turbulence levels computed using the non-conservative $k-\epsilon$ equations.

generalisation are discussed below.

The current shock-unsteadiness model is applied to predict flow separation in SBLI flows in Refs. 20 and 32. The variation of shock strength in the interaction region is computed in terms of the local upstream Mach number normal to the shock wave. It is shown that model parameters based on an average shock strength can yield satisfactory results. The turbulence model equations can thus be transformed into equivalent conservation form using representative average values of c_0 and c_1. The same is true for other turbulence models, like the stress-limited $k-\omega$ model, which prescribe constant values for the model parameters.

In flow applications where gradient-based production is important, the new formulation can be combined with the standard form of the turbulence model. An appropriate blending can be devised, such that the conservation form is solved in high-compression regions and the original form of the equations is retained elsewhere in the flow domain. This has been achieved successfully for applying the shock-unsteadiness correction only in the vicinity of shock waves, using a shock-identifier function.[19] A similar approach can be used here for the conservative formulation.

V. Conclusions

The paper presents application of the $k-\epsilon$ turbulence model to the interaction of homogeneous isotropic turbulence with normal shock waves. The numerical predictions are compared with available DNS data and results of linear interaction analysis. It is shown that the non-conservative source terms in the $k-\epsilon$ equations can result in non-physical solution for strong shock waves. There is excessive amplification of turbulent dissipation rate at high Mach numbers, which can cause rapid decay of the downstream turbulence. An alternate formulation of the $k-\epsilon$ equations is proposed, which eliminates the non-conservative source terms.

The corresponding results match DNS amplification of turbulent kinetic energy and its dissipation rate. Also, the prediction of the conservative $k-\epsilon$ equations approaches the exact inviscid solution and linear theory results with successive grid refinement. The new formulation thus yields significant improvement over the conventional turbulence model equations, and forms the basis for further application to shock-boundary layer interaction flows.

Acknowledgements

The authors wish to acknowledge Prof. Johan Larsson of University of Maryland for providing the DNS data for model evaluation.

References

[1] Coakley, T. J., and Huang, P. G., "Turbulence Modeling for High Speed Flows," AIAA Paper 1992-0436, Jan. 1992.

[2] Horstman, C. C., "Prediction of Hypersonic Shock-Wave/Turbulent Boundary-Layer Flows," AIAA Paper 1987-1367, June 1987.

[3] Huang, P. G., and Coakley, T. J., "Turbulence Modeling for Complex Hypersonic Flows," AIAA Paper 1993-0200, Jan. 1993.

[4] Barakos, G., and Drikakis, D., "Assessment of Various low-Reynolds Number Turbulence Models in Shock-boundary Layer Interaction," *Computer Methods in Applied Mechanics and Engineering*, Vol. 160, No. 1, 1998, pp. 155-174.

[5] Knight, D., Yan, H., Panaras, A.G., and Zheltovodov, A., "Advances in CFD Prediction of Shock Wave Turbulent Boundary Layer Interactions," *Progress in Aerospace Sciences*, Vol. 39, Issues 2-3, 2003, pp. 121-184.

[6] Roy, C. J., and Blottner, F. G., "Review and Assessment of Turbulence Models for Hypersonic Flows," *Progress in Aerospace Sciences*, Vol. 42, Issues 7-8, 2006, pp. 469-530.

[7] Lee, S., Lele, S. K. and Moin, P., "Direct Numerical Simulation of Isotropic Turbulence Interacting with a Weak Shock Wave," *Journal of Fluid Mechanics.*, Vol. 251, 1993, pp. 533-562.

[8] Mahesh, K., Lele, S. K., and Moin, P., "The Influence of Entropy Fluctuations on the Interaction of Turbulence with a Shock Wave," *Journal of Fluid Mechanics*, Vol. 334, 1997, pp. 353-379.

[9] Jamme, S., Cazalbou, J. B., Torres, F. and Chassaing, P., "Direct Numerical Simulation of the Interaction Between a Shock Wave and Various Types of Isotropic Turbulence," *Flow, Turbulence and Combustion*, Vol. 68, 2002, pp. 227-268.

[10] Larsson, J., and Lele, S. K., "Direct Numerical Simulation of Canonical Shock/Turbulence Interaction," *Physics of Fluids*, Vol. 21, 2009, pp. 126101.

[11] Durbin, P. A., and Zeman, O., "Rapid Distortion Theory for Homogeneous Compressed Turbulence with Application to Modelling," *Journal of Fluid Mechanics*, Vol. 242, 1992, pp. 349-370.

[12] Cambon, C., Coleman, G. N., and Mansour, N. N., "Rapid Distortion Analysis and Direct Simulation of Compressible Homogeneous Turbulence at Finite Mach Number," *Journal of Fluid Mechanics*, Vol. 257, 1993, pp. 641-665.

[13] Mahesh, K., Moin, P., and Lele, S. K., "The Interaction of a Shock Wave with a Turbulent Shear Flow," Thermosciences Division, Department of Mechanical Engineering, Stanford University, *Report* TF-69, Stanford, CA, 1996.

[14] Wouchuk, J., Huete Ruiz de Lira, C., and Velikovich, A., "Analytical Linear Theory for the Interaction of a Planar Shock Wave with an Isotropic Turbulent Vorticity Field," *Physical Review E*, Vol. 79, No. 6, 2009.

[15] Barre, S., Alem, D., and Bonnet, J. P., "Experimental Study of a Normal Shock/Homogeneous Turbulence Interaction," *AIAA Journal*, Vol. 34. No. 5, 1996, pp. 968-974.

[16] Sinha, K., Mahesh, K., and Candler, G. V., "Modeling Shock-Unsteadiness in Shock/Turbulence Interaction," *Physics of Fluids*, Vol. 15, No. 8, 2003, pp. 2290-2297.

[17] Veera, V. K., and Sinha, K., "Modeling the Effect of Upstream Temperature Fluctuations on Shock/homogeneous Turbulence Interaction." *Physics of Fluids*, Vol. 21, 2009, pp. 025101..

[18] Sinha, K., "The Evolution of Enstrophy in Shock/Homogeneous Turbulence Interaction," *Journal of Fluid Mechanics*, Vol. 707, 2012, pp. 74-110.

[19] Sinha, K., Mahesh, K., and Candler, G. V., "Modeling the Effect of Shock-Unsteadiness in Shock/Turbulent Boundary-Layer Interactions," *AIAA Journal*, Vol. 43, No. 3, 2005, pp. 586-594.

[20] Pasha, A. A., and Sinha, K., "Simulation of Hypersonic Shock/Turbulent Boundary-Layer Interactions Using Shock-Unsteadiness Model," *Journal of Propulsion and Power*, Vol. 28, No. 1, 2012, pp. 46-60.

[21] Sarkar, S., Erlebacher, G., Hussaini, M.Y., and Kreiss, H.O., "The Analysis and Modelling of Dilatational Terms in Compressible Turbulence," *Journal of Fluid Mechanics*, Vol. 227, 1991, pp. 473-493.

[22] Haidinger, F. A., and Friedrich, R., "Computation of Shock Wave Turbulent Boundary Layer Interactions Using a Two Equation Model with Compressibility Corrections," *Applied Scientific Research*, Vol. 51, Nos. 1-2, 1993, pp. 501-505.

[23] Thivet, F., Knight, D.D., Zheltovodov, A.A., and Maksimov, A.I., "Importance of Limiting the Turbulent Stresses to Predict 3D Shock-wave Boundary-layer Interactions," 23rd International Symposium on Shock Waves, Fort Worth, TX, Paper No. 2761, 2001.

[24] Wilcox, D. C., "Formulation of the $k-\omega$ Turbulence Model Revisited," *AIAA Journal*, Vol. 46, No. 11, 2008, pp. 2823-2838.

[25] Wilcox, D.C., *Turbulence modeling for CFD*, DCW Industries, Inc., La Canada, CA, 1998, pp. 236-239.

[26] Menter, F. R., "Two-Equation Eddy-Viscosity Turbulence Models for Engineering Applications," *AIAA Journal*, Vol. 32, No. 8, 1994, pp. 1598-1605.

[27] Durbin, P.A., "On the k-3 stagnation point anomaly," *Int. J. of Heat Fluid Flow*, Vol. 17, 1996, pp. 89-90.

[28] Shih, T.H., Liou, W.W., Shabbir, A., Yang, Z., and Zhu,J., "A new $k-\epsilon$ eddy viscosity model for high Reynolds number turbulent flows," *Comput. Fluids*, Vol. 24, No. 3, 1997, pp. 227-238.

[29] Sinha, K., and Candler, G. V., "Convergence Improvement of Two-equation Turbulence Model Calculations," AIAA Paper 1998-2649, June 1998.

[30] MacCormack, R. W., and Candler, G. V., "The Solution of the Navier-Stokes Equations Using Gauss-Siedel Line Relaxation," *Computers and Fluids*, Vol. 17, Issue 1, 1989, pp. 135-150.

[31] Wright, M. J., Candler, G. V., and Bose, D., "Data-Parallel Line Relaxation Method for the Navier-Stokes Equations," *AIAA Journal*, Vol. 36, No. 9, 1998, pp. 1603-1609.

[32] Pasha, A. A., and Sinha, K., "Shock-Unsteadiness Model Applied to Oblique Shock-Wave/Turbulent Boundary-Layer Interaction," *International Journal of Computational Fluid Dynamics*, Vol. 22, No. 8, 2008, pp. 569-582.

A Appendix

This appendix presents the discretization error for an equation of the form

$$\frac{\partial h}{\partial x} = \psi \tag{A.1}$$

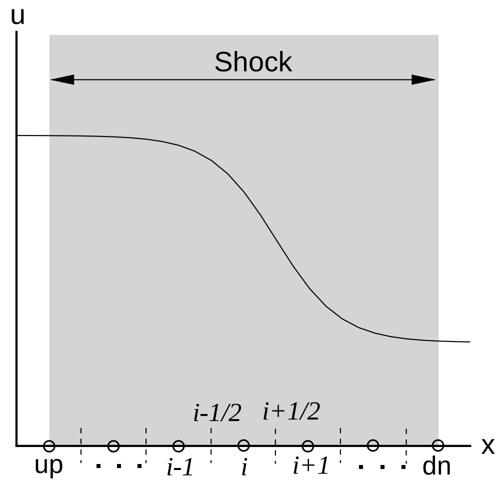

Figure 9: Finite volume grid for discretization of fluxes and source terms in the region of a flow discontinuity.

in the region of a flow discontinuity. Here, h represents the convective flux, for example, $\bar{\rho}\tilde{u}k$ in (5), and ψ is a non-conservative source term, like the production in the k-equation

$$\psi = -\frac{2}{3} c_0 \bar{\rho} k \frac{\partial \tilde{u}}{\partial x} \tag{A.2}$$

The convective and production terms in the ϵ-equation can also be cast in the above form.

The convective term on the left-hand side is discretized in terms of the fluxes evaluated at the cell interfaces. For the ith cell (see Fig. 9),

$$\frac{\partial h}{\partial x} \simeq \frac{h_{i+1/2} - h_{i-1/2}}{\Delta x} \tag{A.3}$$

An upwind-biased method is usually employed to compute the fluxes $h_{i+1/2}$ and $h_{i-1/2}$. Using Taylor series to expand the right-hand side gives

$$\left(\frac{\partial h}{\partial x}\right)_i + \frac{1}{3}\frac{\Delta x^2}{8}\left(\frac{\partial^3 h}{\partial x^3}\right)_i + \ldots\,, \tag{A.4}$$

where the second term is the leading-order truncation error. On integration over the finite volume cell, we get

$$\left[h_{i+1/2} - h_{i-1/2}\right] + \frac{\Delta x^2}{24}\left[\left(\frac{\partial^2 h}{\partial x^2}\right)_{i+1/2} - \left(\frac{\partial^2 h}{\partial x^2}\right)_{i-1/2}\right] + \ldots\,, \tag{A.5}$$

where the integrated error is a function of the derivatives evaluated at the cell interfaces.

The source term ψ involves non-conservative derivative of the shock-normal flow velocity. A symmetric second-order discretization of the velocity derivative yields

$$\psi \simeq -\frac{2}{3}c_0\bar{\rho}k\left(\frac{\tilde{u}_{i+1}-\tilde{u}_{i-1}}{2\Delta x}\right) \tag{A.6}$$

$$= -\frac{2}{3}c_0\bar{\rho}k\left[\left(\frac{\partial\tilde{u}}{\partial x}\right)_i + \frac{\Delta x^2}{3}\left(\frac{\partial^3\tilde{u}}{\partial x^3}\right)_i + \ldots\right], \tag{A.7}$$

where Taylor series expansion is used again to identify the leading-order error. Integration over the finite volume cell gives

$$-\frac{2}{3}c_0\int_{x_{i-1/2}}^{x_{i+1/2}} \bar{\rho}k\frac{\partial\tilde{u}}{\partial x}dx - \frac{2}{3}c_0\frac{\Delta x^2}{3}\int_{x_{i-1/2}}^{x_{i+1/2}} \bar{\rho}k\frac{\partial^3\tilde{u}}{\partial x^3}dx - \ldots \tag{A.8}$$

Here, the first term represents the integrated production of TKE in the cell, and the second term is the discretization error.

If the solution is continuous, then the derivatives are finite and the magnitude of error decreases monotonically as the grid is refined. This is not true in regions of flow discontinuity. The shock thickness computed using a shock-capturing method decreases with successive grid refinement, such that the derivative

$$\frac{\partial\tilde{u}}{\partial x} \sim \frac{\Delta\tilde{u}}{\Delta x} \sim \frac{\Delta\tilde{u}}{\delta},$$

where $\Delta\tilde{u}$ is the jump in the flow variable across the shock, Δx is the grid spacing and δ is the computed shock thickness. The higher-order derivatives scale as

$$\frac{\partial^2\tilde{u}}{\partial x^2} \sim \frac{\Delta\tilde{u}}{\delta^2} \quad \text{and} \quad \frac{\partial^3\tilde{u}}{\partial x^3} \sim \frac{\Delta\tilde{u}}{\delta^3} \tag{A.9}$$

and are therefore unbounded in the limit $\Delta x \to 0$.

The total error accrued in the region of a shock wave can be estimated when the contributions of all the cells spanning the shock are taken together (see Fig. 9). Summation of the conservative flux terms (A.5) for all the cells between x_{up} and x_{dn} gives

$$[h_{dn} - h_{up}] + \frac{\Delta x^2}{24}\left[\left(\frac{\partial^2 h}{\partial x^2}\right)_{dn} - \left(\frac{\partial^2 h}{\partial x^2}\right)_{up}\right] + \ldots, \tag{A.10}$$

where the leading error term involves derivatives evaluated outside the region of discontinuous solution, and is therefore small in magnitude. Similarly, the discretized source term (A.8) for all the cells add up to

$$-\frac{2}{3}c_0\int_{x_{up}}^{x_{dn}} \bar{\rho}k\frac{\partial\tilde{u}}{\partial x}dx - \frac{2}{3}c_0\frac{\Delta x^2}{3}\int_{x_{up}}^{x_{dn}} \bar{\rho}k\frac{\partial^3\tilde{u}}{\partial x^3}dx - \ldots, \tag{A.11}$$

where the non-conservative error term involves higher-order derivatives evaluated in the region of the shock wave. The derivatives attain large values, as per (A.9), and the integrated error remains finite as the grid is refined. In some cases, for example, strong shock waves, it can be comparable or larger than the production term in magnitude.